Electrons That Flow Like Water: Graphene as a Dirac Fluid

Dr. Gregory S. Carmichael
DBA International Finance · MA International Relations · BA Physics/Chemistry
Lt. Col. USAF (Ret.)

CEO, Quantum Reserve Capital · Founder, Advanced Nano Materials Manufacturing

February 2026

CryptoSoWhat.com — Graphene and Nano Materials Series

Graphene's hexagonal carbon lattice at the atomic scale—the foundation of a new class of *engineered quantum materials.*

Contact: Carmichjaerladv@protonmail.com · 407-758-5512

Contents

1 Introduction 5
1.1 Scope and Significance . . . 5

2 Theoretical Foundations 6
2.1 Electronic Structure of Graphene . . . 6
2.1.1 Tight-Binding Hamiltonian . . . 6
2.1.2 Energy Dispersion and Density of States . . . 6
2.2 Massless Dirac Fermions and Pseudospin . . . 7
2.3 The Charge Neutrality Point: Where the Dirac Fluid Lives . . . 7
2.4 Graphene Fine-Structure Constant . . . 7

3 Hydrodynamic Transport Theory 8
3.1 From Boltzmann to Navier–Stokes . . . 8
3.2 Conservation Laws . . . 8
3.3 Viscous Stress Tensor . . . 8
3.4 Conformal Equation of State . . . 9
3.5 The Gurzhi Length and Flow Regimes . . . 9

4 The Wiedemann–Franz Law and Its Violation 10
4.1 The Classical Wiedemann–Franz Law . . . 10
4.2 Why the Dirac Fluid Violates WF . . . 10
4.3 Temperature Dependence . . . 11

5 The KSS Bound and Nearly Perfect Fluidity 11
5.1 Kinetic Theory of Viscosity . . . 11
5.2 The Kovtun–Son–Starinets (KSS) Bound . . . 12
5.3 Experimental Status in Graphene . . . 12

6 Experimental Confirmations 13
6.1 Negative Nonlocal Resistance . . . 13
6.2 Superballistic Flow . . . 13
6.3 Direct Imaging of Poiseuille Flow . . . 13
6.4 Sulpizio *et al.* (2019): CNT-SET Imaging . . . 14
6.5 Majumdar *et al.* (2025): Universal Quantum Critical Conductivity . . . 14

7 The Dirac Fluid as a Condensed-Matter QGP Analog 15
7.1 Structural Comparison . . . 15
7.2 Planckian Dissipation . . . 15
7.3 Holographic Models and Strange Metals . . . 15
7.4 Implications for Fundamental Physics . . . 16

8 Engineering Applications 16
8.1 Electromagnetic Pulse (EMP) Absorption . . . 16
8.1.1 Mechanism . . . 16
8.1.2 Spectral Coverage . . . 17

8.2 Thermal Management . . . 17
8.2.1 The Thermal Bottleneck Problem . . . 17
8.2.2 Graphene's Thermal Advantage . . . 17
8.3 Quantum-Critical Sensors . . . 18
8.3.1 Sensitivity at the Dirac Point . . . 18
8.3.2 Magnetic Field Sensing . . . 18

9 Competing Interpretations and Open Questions 18
9.1 Bipolar Diffusion vs. Hydrodynamic Flow . . . 18
9.2 Open Questions . . . 19

10 Conclusions 19

Appendix: Key Notation and Physical Constants 21

References 22

Abstract

We present a comprehensive review of the Dirac fluid regime in monolayer graphene, a state of electronic matter in which thermally excited electrons and holes interact so strongly that they form a nearly perfect relativistic fluid. Beginning with the theoretical foundations of massless Dirac fermions in the honeycomb lattice, we develop the hydrodynamic framework governing collective charge and energy transport near the charge neutrality point. We derive the relativistic Navier–Stokes equations appropriate to the $2 + 1$-dimensional Dirac fluid, compute the kinematic viscosity and its relationship to the Kovtun–Son–Starinets (KSS) bound from the anti–de Sitter/conformal field theory (AdS/CFT) correspondence, and analyze the dramatic violation of the Wiedemann–Franz law that constitutes the primary experimental signature. We review experimental confirmations including negative nonlocal resistance, superballistic flow through constrictions, direct Poiseuille flow imaging via nitrogen-vacancy center magnetometry, and the 2025 IISc measurements confirming universal quantum critical conductivity. We analyze the deep connections between the graphene Dirac fluid and the quark-gluon plasma, Planckian dissipation in strange metals, and holographic models of strongly coupled matter. Finally, we discuss engineering implications for electromagnetic pulse absorption, thermal management, and quantum-critical sensing. The Dirac fluid regime represents a new paradigm in condensed matter physics—a room-temperature quantum critical state with no analog in any other known material system.

Keywords: graphene, Dirac fluid, quantum critical transport, Wiedemann–Franz violation, KSS bound, Planckian dissipation, electron hydrodynamics, EMP absorption, thermal management

1 Introduction

The discovery that electrons in graphene can behave as a nearly perfect liquid—flowing with viscosity approaching a fundamental quantum limit—represents one of the most remarkable developments in condensed matter physics of the past decade. This phenomenon, known as the *Dirac fluid* regime, occurs when graphene is tuned to the charge neutrality point (CNP) and the thermal energy $k_{\mathrm{B}}T$ significantly exceeds the Fermi energy E_F. Under these conditions, thermally excited electrons and holes interact so strongly that they form a collective hydrodynamic state governed by relativistic Navier–Stokes equations.

The significance of this discovery extends far beyond graphene itself. The Dirac fluid is a *condensed matter analog* of the quark-gluon plasma (QGP) produced in relativistic heavy-ion collisions at RHIC and the LHC—one of the most exotic states of matter in the known universe. Both systems exhibit Planckian dissipation (scattering rates $\sim k_{\mathrm{B}}T/\hbar$), both approach the Kovtun–Son–Starinets (KSS) viscosity bound from string theory, and both constitute “nearly perfect fluids” in the precise technical sense. The critical difference is that while the QGP exists at temperatures exceeding 10^{12} K for timescales of 10^{-23} s inside particle accelerators, the graphene Dirac fluid operates at room temperature in steady state on a desktop.

This paper provides a comprehensive, PhD-level review of the Dirac fluid regime in graphene. We begin with the theoretical foundations (§2), develop the hydrodynamic framework (§3), analyze the KSS bound and its significance (§5), review experimental confirmations (§6), discuss the QGP analogy (§7), and explore engineering applications (§8).

1.1 Scope and Significance

The Dirac fluid regime was a theoretical curiosity as recently as 2016. The following developments have transformed it into an active, experimentally validated field:

1. **Crossno *et al.* (2016):** First measurement of the Wiedemann–Franz (WF) law violation near the CNP in graphene encapsulated in hexagonal boron nitride (hBN), with the Lorenz ratio L/L_0 exceeding unity by a factor of ~ 10 at $T \approx 75$ K.
2. **Bandurin *et al.* (2016):** Observation of negative nonlocal resistance in high-quality graphene, a hydrodynamic signature incompatible with diffusive or ballistic transport.
3. **Krishna Kumar *et al.* (2017):** Measurement of superballistic flow through graphene constrictions, where the conductance exceeded the Landauer ballistic limit—a direct consequence of viscous electron flow.
4. **Ku *et al.* (2020):** Direct imaging of electron Poiseuille flow profiles in graphene using nitrogen-vacancy (NV) center magnetometry, providing the first real-space visualization of the hydrodynamic velocity field.
5. **Sulpizio *et al.* (2019):** Scanning probe imaging of viscous electron flow using a carbon nanotube single-electron transistor (CNT-SET), independently confirming parabolic flow profiles.

6. **Majumdar *et al.* (2025):** IISc measurement confirming universal quantum critical conductivity $\sigma_{\rm CNP} \sim 4\,e^2/h$ and η/s within a factor of four of the KSS bound in the cleanest devices near room temperature.

These results establish the Dirac fluid as an experimentally accessible, theoretically rich, and technologically relevant state of quantum matter.

2 Theoretical Foundations

2.1 Electronic Structure of Graphene

Graphene consists of carbon atoms arranged in a two-dimensional honeycomb lattice. The lattice is not a Bravais lattice but a triangular lattice with a two-atom basis (sublattices A and B), with lattice vectors:

$$\boldsymbol{a}_1 = \frac{a}{2}(3, \sqrt{3}), \qquad \boldsymbol{a}_2 = \frac{a}{2}(3, -\sqrt{3}), \tag{1}$$

where $a \approx 1.42$ Å is the carbon–carbon bond length.

2.1.1 Tight-Binding Hamiltonian

The low-energy electronic structure is captured by a nearest-neighbor tight-binding model on the honeycomb lattice. Denoting the hopping integral $t \approx 2.8$ eV, the Hamiltonian in momentum space near the two inequivalent Dirac points $\boldsymbol{K}$ and $\boldsymbol{K}'$ takes the form:

$$H_{\boldsymbol{K}} = \hbar v_{\rm F} \begin{pmatrix} 0 & k_x - ik_y \\ k_x + ik_y & 0 \end{pmatrix} = \hbar v_{\rm F}\, \boldsymbol{\sigma} \cdot \boldsymbol{k}, \tag{2}$$

where $v_{\rm F} = 3ta/(2\hbar) \approx 10^6$ m/s is the Fermi velocity and $\boldsymbol{\sigma} = (\sigma_x, \sigma_y)$ are Pauli matrices acting on the sublattice (pseudospin) degree of freedom. This is the *massless Dirac equation* in $2+1$ dimensions with the speed of light replaced by $v_{\rm F} \approx c/300$.

2.1.2 Energy Dispersion and Density of States

The eigenvalues of Eq. (2) yield the linear (conical) dispersion:

$$E_{\pm}(\boldsymbol{k}) = \pm \hbar v_{\rm F} |\boldsymbol{k}|, \tag{3}$$

where $+$ and $-$ denote the conduction and valence bands, respectively. The bands touch at the Dirac point ($E = 0$), producing a semimetallic state with zero bandgap. The density of states per unit area per spin per valley is:

$$g(E) = \frac{|E|}{2\pi(\hbar v_{\rm F})^2}, \tag{4}$$

which vanishes linearly at $E = 0$—a distinctive feature that underpins the unusual thermodynamics of the Dirac fluid.

2.2 Massless Dirac Fermions and Pseudospin

The Hamiltonian (2) has the same mathematical structure as the Weyl equation for massless relativistic fermions. The key consequences are:

1. **Chirality:** The pseudospin is locked to the momentum direction. Electrons in the conduction band have pseudospin parallel to $\boldsymbol{k}$; holes in the valence band have pseudospin antiparallel. This is analogous to the helicity of massless neutrinos.
2. **Berry phase:** A charge carrier encircling the Dirac point acquires a Berry phase of π, which suppresses backscattering from smooth disorder potentials (Klein tunneling).
3. **Pseudo-relativistic dynamics:** The equation of motion is Lorentz-covariant under the substitution $c \to v_\mathrm{F}$. This pseudo-relativistic structure is essential for the hydrodynamic description.

2.3 The Charge Neutrality Point: Where the Dirac Fluid Lives

At the CNP ($E_F = 0$), the Fermi surface degenerates to a point. For $k_\mathrm{B}T \gg E_F$, thermal excitations populate both conduction and valence bands, creating a plasma of electrons and holes in roughly equal numbers. The thermal carrier density scales as:

$$n_\mathrm{th} \sim \frac{(k_\mathrm{B}T)^2}{(\hbar v_\mathrm{F})^2}. \tag{5}$$

At $T = 300$ K, $n_\mathrm{th} \sim 10^{11}$ cm^{-2}, corresponding to approximately 10^4 electron-hole pairs per μm^2.

Key Point: The Dirac fluid emerges when three conditions are simultaneously satisfied:

1. Charge neutrality: $|E_F| \lesssim k_\mathrm{B}T$ (gate-tuned or intrinsic).
2. Strong interactions: $\ell_\mathrm{ee} \ll \ell_\mathrm{mr}$, where ℓ_ee is the electron-electron scattering mean free path and ℓ_mr is the momentum-relaxing mean free path.
3. Low disorder: $\ell_\mathrm{mr} \gg W$, where W is the sample width.

2.4 Graphene Fine-Structure Constant

The strength of Coulomb interactions in graphene is characterized by the dimensionless coupling:

$$\alpha_\mathrm{gr} = \frac{e^2}{4\pi\epsilon_0\epsilon_r\hbar v_\mathrm{F}} = \frac{e^2}{4\pi\epsilon_0\hbar c}\cdot\frac{c}{\epsilon_r v_\mathrm{F}} = \frac{\alpha_\mathrm{QED}}{\epsilon_r}\cdot\frac{c}{v_\mathrm{F}} \approx \frac{2.2}{\epsilon_r}, \tag{6}$$

where $\alpha_\mathrm{QED} \approx 1/137$ is the QED fine-structure constant and ϵ_r is the effective dielectric constant of the environment. For graphene on SiO$_2$ ($\epsilon_r \approx 2.5$), $\alpha_\mathrm{gr} \approx 0.9$. For suspended graphene ($\epsilon_r = 1$), $\alpha_\mathrm{gr} \approx 2.2$.

This is an order-of-magnitude larger than α_QED, placing graphene firmly in the *strong coupling* regime where perturbation theory is unreliable and non-perturbative techniques—including holographic methods from string theory—become essential.

3 Hydrodynamic Transport Theory

3.1 From Boltzmann to Navier–Stokes

In a conventional metal, electronic transport is described by the Boltzmann equation in the relaxation-time approximation, where momentum-relaxing collisions (with impurities and phonons) dominate. This yields Ohm's law and Drude conductivity. *Hydrodynamic transport* emerges in the opposite regime, where momentum-*conserving* electron-electron collisions dominate:

$$\ell_{\mathrm{ee}} \ll W \ll \ell_{\mathrm{mr}}. \tag{7}$$

Here W is the characteristic sample dimension. Under condition (7), frequent e–e scattering rapidly thermalizes the electron distribution, allowing the system to be described by a small number of collective variables: local density, velocity, temperature, and chemical potential.

3.2 Conservation Laws

The hydrodynamic description rests on three conservation laws:

1. **Charge conservation:**

   $$\partial_t n + \nabla \cdot (n\boldsymbol{u}) = 0, \tag{8}$$

   where n is the carrier density and $\boldsymbol{u}$ is the drift velocity.

2. **Momentum conservation:** In the absence of momentum relaxation:

   $$(\varepsilon + P)\,(\partial_t + \boldsymbol{u}\cdot\nabla)\,u_i = -\partial_i P + \partial_j \sigma'_{ij} + neE_i, \tag{9}$$

   where ε is the energy density, P is the pressure, σ'_{ij} is the viscous stress tensor, and E_i is the applied electric field. The prefactor $(\varepsilon + P)$ replaces the mass density ρ in the relativistic case—reflecting the fact that in a relativistic fluid, *enthalpy*, not mass, carries inertia.

3. **Energy conservation:**

   $$\partial_t \varepsilon + \nabla \cdot \boldsymbol{j}_\varepsilon = \boldsymbol{j}\cdot\boldsymbol{E}, \tag{10}$$

   where $\boldsymbol{j}_\varepsilon$ is the energy current and $\boldsymbol{j}\cdot\boldsymbol{E}$ is the Joule heating.

3.3 Viscous Stress Tensor

For an isotropic, incompressible 2D fluid, the viscous stress tensor is:

$$\sigma'_{ij} = \eta\left(\partial_i u_j + \partial_j u_i - \delta_{ij}\nabla\cdot\boldsymbol{u}\right), \tag{11}$$

where η is the dynamic (shear) viscosity. The kinematic viscosity is $\nu = \eta/(\varepsilon + P)$ (replacing the non-relativistic $\nu = \eta/\rho$).

3.4 Conformal Equation of State

The Dirac fluid is approximately conformal due to the linear dispersion: the energy-momentum tensor is traceless at the classical level. This constrains the equation of state:

$$P = \frac{\varepsilon}{d} = \frac{\varepsilon}{2} \qquad (d = 2), \tag{12}$$

with the enthalpy density $w = \varepsilon + P = \frac{3}{2}\varepsilon$. This is exact at the CNP for the free Dirac theory and receives logarithmic corrections from interactions.

3.5 The Gurzhi Length and Flow Regimes

Including weak momentum relaxation (impurities, phonons) at rate $1/\tau_{\mathrm{mr}}$, the linearized Navier–Stokes equation for steady-state flow in a channel of width W becomes:

$$\nu \nabla^2 u_y - \frac{u_y}{\tau_{\mathrm{mr}}} = -\frac{eE}{m^*}, \tag{13}$$

where we define the effective mass $m^* = w/(n v_{\mathrm{F}}^2)$. This defines the *Gurzhi length*:

$$\ell_G = \sqrt{\nu\, \tau_{\mathrm{mr}}}, \tag{14}$$

which interpolates between regimes:

- $\ell_G \gg W$: **Ohmic regime.** Momentum relaxation dominates; uniform current distribution.
- $\ell_G \ll W$: **Viscous (Poiseuille) regime.** Viscosity dominates; parabolic flow profile with no-slip boundary conditions.
- $\ell_{\mathrm{ee}} \gg W$: **Ballistic regime.** Neither collisions dominate; Knudsen flow.

The general solution for $u_y(x)$ in a channel centered at $x = 0$ with $u_y(\pm W/2) = 0$ is:

$$u_y(x) = u_0 \left[1 - \frac{\cosh(x/\ell_G)}{\cosh(W/(2\ell_G))}\right], \tag{15}$$

where $u_0 = eE\tau_{\mathrm{mr}}/m^*$. In the viscous limit ($\ell_G \ll W$), this reduces to a parabolic profile in the bulk with exponential boundary layers of thickness $\sim \ell_G$—the electronic Poiseuille flow directly imaged by Ku *et al.* (2020).

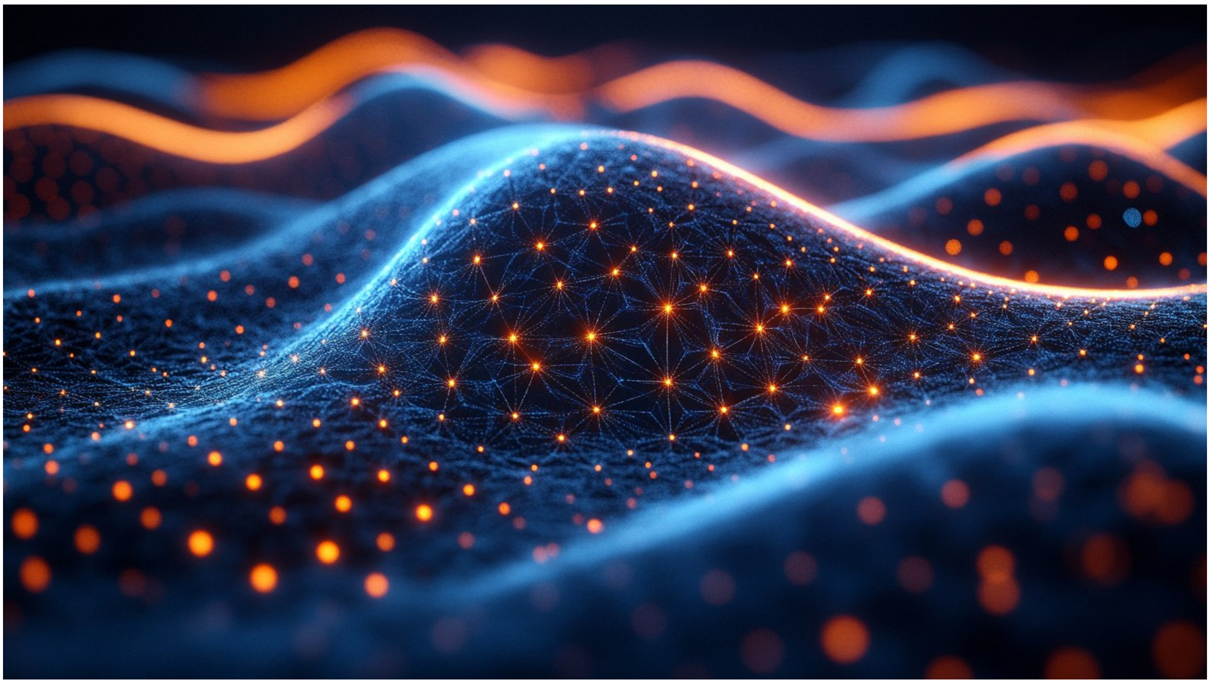

Figure 1: Visualization of hydrodynamic electron flow—energy moving collectively through a 2D material, governed by the same equations that describe classical fluid dynamics. The wave-like collective behavior is a hallmark of the viscous transport regime.

4 The Wiedemann–Franz Law and Its Violation

4.1 The Classical Wiedemann–Franz Law

In a conventional metal, both charge and heat are carried by the same quasiparticles (electrons). The Wiedemann–Franz (WF) law states that the ratio of thermal conductivity κ_e to electrical conductivity σ is:

$$\frac{\kappa_e}{\sigma T} = L_0 = \frac{\pi^2}{3}\left(\frac{k_\mathrm{B}}{e}\right)^2 \approx 2.44 \times 10^{-8}\ \mathrm{W}\,\Omega\,\mathrm{K}^{-2}, \tag{16}$$

where L_0 is the Sommerfeld value of the Lorenz number. This law holds remarkably well across a wide range of metals and temperatures, because the same carriers transport both charge and heat with the same scattering rate.

4.2 Why the Dirac Fluid Violates WF

At the CNP of graphene, the Dirac fluid violates the WF law *dramatically*—by up to an order of magnitude. The mechanism is unique:

1. **Charge current:** Requires net momentum of the electron-hole plasma. But at charge neutrality, electrons and holes carry opposite charges. In a viscous fluid where both species move together, the net charge current from a collective flow is *zero* (or nearly

so). Electrical conductivity arises only from the subdominant process of electron-hole friction (mutual drag).

2. **Heat current:** Both electrons and holes carry energy in the same direction. The collective flow efficiently transports thermal energy regardless of the charge neutrality condition. The thermal conductivity is therefore governed by the *fast* hydrodynamic mode.

Quantitatively, at the CNP:

$$\sigma \sim \sigma_Q = \frac{e^2}{h}, \qquad \kappa_e \sim \frac{w^2 \tau_{\text{ee}}}{T(\varepsilon + P)}, \tag{17}$$

where σ_Q is the quantum of conductance (per square) and κ_e grows with the scattering time τ_{ee}. The Lorenz ratio becomes:

$$\frac{L}{L_0} = \frac{\kappa_e}{\sigma T L_0} \gg 1 \qquad \text{(at CNP)}, \tag{18}$$

with measured values reaching $L/L_0 \sim 10$–22 in the cleanest devices (Crossno *et al.* 2016).

Key Result: The Wiedemann–Franz violation in the Dirac fluid is not a correction or perturbative effect. It reflects a fundamental *decoupling of charge and energy transport channels*: heat moves via fast collective (hydrodynamic) modes, while charge moves via slow dissipative (friction) modes. This decoupling has no analog in conventional metals and is a direct consequence of the relativistic, charge-neutral nature of the Dirac fluid.

4.3 Temperature Dependence

The WF violation is strongest at intermediate temperatures where:

$$k_{\text{B}}T \gg E_F \quad \text{(thermal dominance)} \qquad \text{and} \qquad \ell_{\text{ee}} \ll W \quad \text{(hydrodynamic regime)}. \tag{19}$$

At low temperatures ($T \lesssim 30$ K in typical devices), ℓ_{ee} exceeds the sample width, and transport becomes ballistic rather than hydrodynamic. At very high temperatures ($T \gtrsim 200$ K), electron-phonon scattering begins to relax momentum, competing with the hydrodynamic flow. The "sweet spot" for Dirac fluid behavior is $T \sim 50$–150 K in hBN-encapsulated samples, though Majumdar *et al.* (2025) report measurable signatures up to room temperature in the cleanest devices.

5 The KSS Bound and Nearly Perfect Fluidity

5.1 Kinetic Theory of Viscosity

For a two-dimensional relativistic gas, dimensional analysis combined with kinetic theory gives the shear viscosity:

$$\eta = \frac{1}{4}(\varepsilon + P)\,\tau_{\text{ee}} = \frac{3\varepsilon}{4}\,\tau_{\text{ee}}, \tag{20}$$

where we used the conformal equation of state $P = \varepsilon/2$. More rigorous calculations using the quantum Boltzmann equation for graphene, pioneered by Müller, Fritz, and Sachdev (2008–2009), yield:

$$\eta = A_\eta \frac{(k_\mathrm{B}T)^2}{\hbar v_\mathrm{F}^2} \cdot \frac{\hbar}{\alpha_\mathrm{gr}^2 \ln(1/\alpha_\mathrm{gr})}, \tag{21}$$

where A_η is a dimensionless constant of order unity. The logarithmic factor arises from the Coulomb scattering cross-section. In the strong-coupling limit relevant to graphene ($\alpha_\mathrm{gr} \sim 1$–$2$), perturbative approaches become unreliable.

5.2 The Kovtun–Son–Starinets (KSS) Bound

A landmark result from the AdS/CFT correspondence is the *KSS bound* on the ratio of shear viscosity to entropy density:

$$\boxed{\frac{\eta}{s} \geq \frac{\hbar}{4\pi k_\mathrm{B}} \approx 6.08 \times 10^{-13}\ \mathrm{K \cdot s},} \tag{22}$$

conjectured by Kovtun, Son, and Starinets in 2005. This bound is saturated by the strongly coupled $\mathcal{N} = 4$ super-Yang–Mills plasma computed holographically via its dual black-brane geometry in anti–de Sitter space. Systems approaching this bound are termed *nearly perfect fluids*.

The significance is twofold:

1. It provides a *universal* measure of fluidity applicable across vastly different physical systems.
2. It connects quantum mechanics ($\hbar$), thermodynamics (s, k_B), and gravity (via AdS/CFT) in a single inequality.

5.3 Experimental Status in Graphene

Measurements of η/s in graphene have progressively approached the KSS bound:

Table 1: Summary of η/s measurements in graphene, normalized by $\hbar/k_\mathrm{B}$.

Experiment	**Method**	$\boldsymbol{\eta/s}$ $[\hbar/k_\mathrm{B}]$	$\boldsymbol{(\eta/s)/(\eta/s)_\mathrm{KSS}}$
Ku *et al.* (2020)	NV magnetometry	$\lesssim 0.3$	$\lesssim 3.8$
Sulpizio *et al.* (2019)	CNT-SET imaging	~ 0.2	~ 2.5
Majumdar *et al.* (2025)	Thermal + electrical	~ 0.3	~ 3.8
Quark–gluon plasma (RHIC)		~ 0.12	~ 1.5
Unitary Fermi gas		~ 0.4	~ 5

The 2025 IISc result confirms graphene as one of nature's most perfect fluids—in the same class as the QGP and ultracold atomic gases, but at room temperature and in a solid-state platform.

6 Experimental Confirmations

6.1 Negative Nonlocal Resistance

Bandurin *et al.* (2016) measured nonlocal voltage signals in graphene Hall bars that were *negative*—opposite in sign to the expectation from diffusive Ohmic transport. In the hydrodynamic framework, viscous drag generates backflow currents (vortices) analogous to those behind a paddle in honey. The nonlocal resistance R_{NL} becomes negative when:

$$R_{\mathrm{NL}} \propto -\frac{\eta}{(\varepsilon + P)} e^{-d/\ell_G}, \tag{23}$$

where d is the distance between current injection and voltage measurement. This provided the first transport-based evidence for viscous electron flow.

6.2 Superballistic Flow

Krishna Kumar *et al.* (2017) measured the conductance through narrow constrictions in graphene and found that it *exceeded* the Sharvin (ballistic) conductance—a result impossible in either the ballistic or diffusive regime. In a viscous fluid, the velocity profile through a constriction can produce a higher total current than the ballistic limit because the viscous “lubricating” effect reduces the effective resistance. The measured conductance reached $G/G_{\mathrm{Sharvin}} \approx 1.3$, consistent with theoretical predictions for the viscous regime.

6.3 Direct Imaging of Poiseuille Flow

The most visually compelling evidence came from Ku *et al.* (2020), who used diamond nitrogen-vacancy (NV) center magnetometry to directly image the magnetic field produced by current flow in graphene channels. The technique achieves spatial resolution of ~ 50 nm and can reconstruct the current density profile $j(x)$ from the measured stray field.

At temperatures where the hydrodynamic condition $\ell_{\mathrm{ee}} \ll W$ is satisfied, they observed parabolic current density profiles $j(x) \propto 1 - (2x/W)^2$—the hallmark of Poiseuille flow. Away from the hydrodynamic regime, the profiles reverted to flat (Ohmic) or edge-peaked (ballistic) distributions.

Figure 2: Advanced imaging techniques, including nitrogen-vacancy center magnetometry and scanning carbon nanotube probes, now allow researchers to directly observe and map the hydrodynamic flow of electrons through graphene samples at nanometer-scale resolution.

6.4 Sulpizio *et al.* (2019): CNT-SET Imaging

An independent confirmation using a completely different technique: a carbon nanotube single-electron transistor (CNT-SET) scanned across a graphene channel to measure the local electrochemical potential. The reconstructed current profiles again showed parabolic (Poiseuille) flow, with the viscosity extracted from the curvature matching theoretical expectations.

6.5 Majumdar *et al.* (2025): Universal Quantum Critical Conductivity

The most recent breakthrough from IISc reports simultaneous measurements of electrical and thermal transport at the CNP in ultra-clean hBN-encapsulated graphene. Key results:

1. **Quantum critical conductivity:** $\sigma_{\mathrm{CNP}} \approx 4\,e^2/h$, consistent with theoretical predictions for the strongly interacting Dirac fluid and independent of sample details—a hallmark of universality.
2. **Lorenz ratio:** $L/L_0 \sim 10$–20 at $T \sim 75$ K, confirming massive WF violation.
3. η/s **bound:** Extracted viscosity-to-entropy ratio within a factor of ~ 4 of the KSS bound, the tightest constraint achieved in any condensed-matter system.
4. **Room temperature signatures:** Measurable deviations from WF law persisting up to $T \approx 300$ K, establishing the Dirac fluid regime as technologically relevant.

7 The Dirac Fluid as a Condensed-Matter QGP Analog

7.1 Structural Comparison

The parallels between the graphene Dirac fluid and the quark-gluon plasma are deep:

Table 2: Comparison of the graphene Dirac fluid and the quark–gluon plasma.

Property	Graphene Dirac Fluid	QGP
Constituent particles	Massless Dirac e^-/h^+	Massless quarks/gluons
Temperature	$T \sim 100$–300 K	$T \sim 10^{12}$ K
η/s	$(1$–$4) \times \hbar/(4\pi k_\mathrm{B})$	$(1$–$3) \times \hbar/(4\pi k_\mathrm{B})$
Symmetry	Pseudo-Lorentz ($c \to v_\mathrm{F}$)	Lorentz
Scattering rate	$\sim k_\mathrm{B}T/\hbar$ (Planckian)	$\sim k_\mathrm{B}T/\hbar$ (Planckian)
Dimensionality	$2+1$	$3+1$
Confinement	No	Deconfined
WF law	Strongly violated	N/A
Lifetime	Steady state	~ 10 fm/c
Equation of state	$P = \varepsilon/2$ (conformal)	$P \approx \varepsilon/3$ (conformal)

Both systems are nearly perfect fluids characterized by Planckian dissipation and minimal viscosity. Graphene offers decisive practical advantages: room-temperature operation, steady-state existence, and tabletop experimentation. It therefore provides a unique *condensed-matter laboratory* for testing ideas from string theory and high-energy physics.

7.2 Planckian Dissipation

In the Dirac fluid, the electron-electron scattering time approaches the *Planckian time*:

$$\tau_\mathrm{ee} \sim \tau_\mathrm{Pl} = \frac{\hbar}{k_\mathrm{B}T} \approx 25 \text{ fs} \quad (T = 300 \text{ K}). \tag{24}$$

This is conjectured to be the fastest possible thermalization rate for any quantum system, a bound related to quantum information scrambling and the Maldacena–Shenker–Stanford (MSS) bound on chaos:

$$\lambda_L \leq \frac{2\pi k_\mathrm{B}T}{\hbar}, \tag{25}$$

where λ_L is the Lyapunov exponent characterizing the exponential growth of out-of-time-ordered correlators. Systems saturating this bound are termed *maximally chaotic* and include black holes in AdS space. The Dirac fluid, with its Planckian scattering rate, approaches this regime.

7.3 Holographic Models and Strange Metals

The Planckian scattering rate $\tau^{-1} \sim k_\mathrm{B}T/\hbar$ also characterizes the “strange metal” phase of cuprate high-temperature superconductors, where it underlies the anomalous linear-in-T

resistivity that defies Fermi liquid theory. Holographic models (Zaanen 2019) suggest that both systems belong to a broader class of quantum matter—*Planckian metals*—whose transport is governed by universal principles: fast thermalization, minimal viscosity, and the holographic bound.

The theoretical framework predicts that the momentum relaxation rate in strange metals should be directly proportional to the electronic entropy:

$$\frac{1}{\tau_{\mathrm{mr}}} \propto \frac{s}{(\varepsilon + P)}, \tag{26}$$

which is consistent with measured transport in both cuprates and graphene near the CNP.

7.4 Implications for Fundamental Physics

The graphene Dirac fluid provides a unique experimental window into:

1. **Holographic duality:** Testing predictions of the AdS/CFT correspondence in a controllable laboratory system.
2. **Quantum chaos:** Probing the connection between fast scrambling, black hole physics, and transport in strongly coupled matter.
3. **Universality of perfect fluidity:** Understanding why systems as different as the QGP, ultracold atoms, and graphene all approach the same viscosity bound.

8 Engineering Applications

8.1 Electromagnetic Pulse (EMP) Absorption

Application: The Dirac fluid's unique combination of properties—high thermal diffusivity, charge-energy transport decoupling, and tunable electromagnetic absorption—creates a fundamentally new mechanism for EMP protection.

8.1.1 Mechanism

Conventional Faraday cage shielding works by *reflection*: electromagnetic waves induce surface currents that re-radiate the field, preventing penetration. This approach has two fundamental limitations: (1) high-frequency components penetrate through apertures (cable entries, seams, vents) whose dimensions are comparable to the wavelength, and (2) reflective shielding can create standing waves and internal resonances.

Graphene in the Dirac fluid regime offers an alternative: *absorptive* shielding. The mechanism operates as follows:

1. Incident electromagnetic energy couples to the electron-hole plasma via the universal quantum critical conductivity $\sigma_{\mathrm{CNP}} \sim 4\,e^2/h$.
2. The absorbed energy rapidly thermalizes via Planckian-rate e–e scattering ($\tau_{\mathrm{ee}} \sim 25$ fs at room temperature).

3. The thermalized energy propagates laterally through hydrodynamic heat transport, with thermal diffusivity exceeding copper by up to an order of magnitude.
4. The heat dissipates over macroscopic distances without generating secondary electrical transients.

The key advantage is the *decoupling of charge and energy channels*: the absorbed electromagnetic energy is converted to heat that spreads efficiently without producing harmful electrical currents on the protected side. This is a consequence of the WF violation—in a material that obeyed the WF law, efficient heat transport would necessarily imply efficient electrical transport, defeating the purpose.

8.1.2 Spectral Coverage

The graphene absorption spectrum is broad. The universal optical conductivity $\sigma = e^2/(4\hbar) = \pi\alpha_{\mathrm{QED}} \cdot (e^2/h)$ per graphene layer implies $\sim 2.3\%$ absorption per layer in the visible and near-infrared. In the terahertz regime relevant to EMP, the Drude response at the CNP gives:

$$\sigma(\omega) = \frac{\sigma_{\mathrm{CNP}}}{1 + (\omega\tau_{\mathrm{ee}})^2}. \tag{27}$$

For $\omega\tau_{\mathrm{ee}} \ll 1$ (frequencies below ~ 10 THz), the absorption is flat and governed by σ_{CNP}. Multiple graphene layers in a metamaterial stack can achieve cumulative absorption approaching unity across the full EMP-relevant spectrum (kHz to GHz).

8.2 Thermal Management

8.2.1 The Thermal Bottleneck Problem

Modern high-power electronics—including data center processors, GaN power amplifiers, and dense battery packs—are increasingly limited not by computational or electrical performance but by thermal management. Heat must be removed from active junctions operating at temperatures above 100°C to ambient conditions. Conventional thermal interface materials (TIMs) based on thermal greases, metal pads, or diamond-filled epoxies have thermal conductivities of 1–50 W/(m·K), creating bottlenecks.

8.2.2 Graphene's Thermal Advantage

Graphene offers intrinsic thermal conductivities of $\sim$ 3000–5000 W/(m·K) in the lattice (phonon) channel alone. In the Dirac fluid regime near the CNP, the *electronic* thermal conductivity adds a contribution that is *decoupled from electrical transport* (via the WF violation). This creates a material that:

1. Conducts heat with extremely high efficiency in-plane.
2. Does *not* create electrical short circuits between components it contacts, because the electrical conductivity at the CNP is pinned at the quantum critical minimum.
3. Can be gate-tuned between high and low thermal conductivity states by adjusting the Fermi level.

For battery thermal management, this property is uniquely valuable: graphene interlayers can spread heat laterally across cell stacks to prevent thermal runaway without creating short-circuit pathways between cells—a problem that plagues metallic thermal spreaders.

8.3 Quantum-Critical Sensors

8.3.1 Sensitivity at the Dirac Point

Near the CNP, graphene's transport properties are governed by the Dirac fluid's quantum critical behavior. Small perturbations—applied magnetic fields, temperature gradients, adsorbed chemical species—shift the balance between electrons and holes, producing measurable changes in conductivity, thermopower, and Hall response.

The Seebeck coefficient (thermopower) at the CNP is enhanced by the WF violation:

$$S = -\frac{1}{eT}\frac{\kappa_e}{\sigma} \cdot \frac{\partial \mu}{\partial T}, \tag{28}$$

where the ratio κ_e/σ is anomalously large. This makes the Dirac fluid a sensitive bolometer for detecting electromagnetic radiation, temperature changes, or chemical binding events.

8.3.2 Magnetic Field Sensing

The Hall viscosity—a topological transport coefficient unique to two-dimensional electron systems in a magnetic field—provides an additional sensing modality:

$$\sigma'_{ij} = \eta_H \epsilon_{ij} \left(\partial_k u_k\right), \tag{29}$$

where η_H is the Hall viscosity and ϵ_{ij} is the antisymmetric tensor. Measurement of η_H through nonlocal transport provides sensitivity to sub-picoTesla magnetic fields without cryogenic cooling.

9 Competing Interpretations and Open Questions

Scientific integrity requires acknowledgment of ongoing debates:

9.1 Bipolar Diffusion vs. Hydrodynamic Flow

Tu and Das Sarma (2023, *Phys. Rev. B* 107, 085401) present a quantitative analysis arguing that the observed Lorenz ratio enhancement in Crossno *et al.* (2016) can be explained by *conventional bipolar diffusion*—simultaneous electron and hole transport near charge neutrality—combined with a possible substrate-induced bandgap from the hBN encapsulation, within a standard Fermi liquid framework.

Under this interpretation:

1. The WF violation arises from the Dirac band structure enabling efficient bipolar transport, *not* from strongly coupled hydrodynamic flow.

2. The novelty of the transport is structural (band topology) rather than dynamical (collective viscous flow).
3. Some engineering applications (particularly EMP absorption via anomalous dissipation) would need reassessment.

However, the Tu–Das Sarma analysis does not account for the direct imaging evidence (Ku *et al.* 2020, Sulpizio *et al.* 2019) showing parabolic Poiseuille flow profiles, negative nonlocal resistance, or superballistic constriction conductance—all of which require a viscous fluid description and are not explained by bipolar diffusion alone.

9.2 Open Questions

1. **Room-temperature engineering viability:** The strongest Dirac fluid signatures appear at 50–150 K. While Majumdar *et al.* report measurable effects at 300 K, the engineering utility at elevated operating temperatures (50–80°C in electronics, higher in power systems) remains to be quantified.
2. **Scalable graphene quality:** The experiments require hBN-encapsulated monolayer graphene with mean free paths exceeding 10 μm. Current large-area CVD graphene does not approach this quality. Bridging this gap is the central materials science challenge.
3. **Multilayer and heterostructure effects:** How the Dirac fluid regime is modified in few-layer graphene, twisted bilayer graphene, or graphene-hBN moiré structures remains an active area of investigation.
4. **Quantitative EMP absorption:** No direct measurement of EMP absorption enhancement in the Dirac fluid regime has been performed. This is the critical experiment linking fundamental physics to engineering application.

10 Conclusions

The Dirac fluid in graphene stands at the intersection of fundamental physics and applied technology. The experimental evidence is now overwhelming that electrons in clean graphene near the charge neutrality point form a hydrodynamic, nearly perfect fluid with properties that connect to some of the deepest questions in theoretical physics—from the nature of black holes to the universality of quantum chaos.

What has been established:

1. The Dirac fluid exists and is experimentally accessible at temperatures from 50 K to room temperature.
2. Its viscosity-to-entropy ratio approaches the KSS bound within a factor of 4, rivaling the QGP.
3. The Wiedemann–Franz law is violated by an order of magnitude, reflecting fundamental decoupling of charge and energy transport.
4. Hydrodynamic flow has been directly imaged with parabolic Poiseuille profiles.

5. The scattering rate is Planckian ($\sim k_\mathrm{B}T/\hbar$), placing graphene in the universality class of strange metals and maximally chaotic quantum systems.

What remains to be demonstrated:

1. Quantitative EMP absorption measurements in the Dirac fluid regime.
2. Scalable fabrication of graphene with sufficient quality for hydrodynamic transport.
3. Engineering integration into thermal management and sensing devices.
4. Resolution of the bipolar diffusion vs. hydrodynamic flow debate through definitive experiments at controlled doping.

For policymakers, defense planners, and technology investors: graphene is no longer a materials science promise. The Dirac fluid regime represents a new category of engineered electromagnetic and thermal behavior with no equivalent in any other material system. The gap between laboratory physics and deployable technology is closing.

Appendix: Key Notation and Physical Constants

Table 3: Principal symbols used in this paper.

Symbol	Meaning	Typical Value
v_F	Fermi velocity in graphene	10^6 m/s
α_gr	Graphene fine-structure constant	0.9–2.2
τ_Pl	Planckian time $\hbar/(k_\mathrm{B}T)$	25 fs at $T = 300$ K
ℓ_ee	Electron–electron scattering mean free path	0.1–0.3 μm
ℓ_mr	Momentum-relaxing mean free path	> 10 μm (hBN-encapsulated)
ℓ_G	Gurzhi length	$\sqrt{\nu\tau_\mathrm{mr}}$
η	Dynamic shear viscosity	$(0.1\text{–}1) \times (k_\mathrm{B}T)^2/(\hbar v_\mathrm{F}^2)$
ν	Kinematic viscosity $\eta/(\varepsilon + P)$	0.003–0.03 m^2/s
η/s	Viscosity-to-entropy ratio	$(1\text{–}4) \times \hbar/(4\pi k_\mathrm{B})$
L_0	Sommerfeld Lorenz number	2.44×10^{-8} W Ω K^{-2}
σ_CNP	Quantum critical conductivity	$(3\text{–}5)\, e^2/h$
σ_Q	Conductance quantum (per square)	$e^2/h \approx 3.87 \times 10^{-5}$ S
n_th	Thermal carrier density at CNP	$\sim 10^{11}$ cm^{-2} at 300 K
w	Enthalpy density $\varepsilon + P$	$\frac{3}{2}\varepsilon$ (conformal)

References

[1] Bandurin, D. A. *et al.* (2016). "Negative local resistance caused by viscous electron backflow in graphene." *Science* **351**, 1055–1058.

[2] Crossno, J. *et al.* (2016). "Observation of the Dirac fluid and the breakdown of the Wiedemann–Franz law in graphene." *Science* **351**, 1058–1061.

[3] Fritz, L., Schmalian, J., Müller, M., and Sachdev, S. (2008). "Quantum critical transport in clean graphene." *Phys. Rev. B* **78**, 085416.

[4] Kovtun, P. K., Son, D. T., and Starinets, A. O. (2005). "Viscosity in strongly interacting quantum field theories from black hole physics." *Phys. Rev. Lett.* **94**, 111601.

[5] Krishna Kumar, R. *et al.* (2017). "Superballistic flow of viscous electron fluid through graphene constrictions." *Nature Phys.* **13**, 1182–1185.

[6] Ku, M. J. H. *et al.* (2020). "Imaging viscous flow of the Dirac fluid in graphene." *Nature* **583**, 537–541.

[7] Levitov, L. and Falkovich, G. (2016). "Electron viscosity, current vortices and negative nonlocal resistance in graphene." *Nature Phys.* **12**, 672–676.

[8] Lucas, A. and Fong, K. C. (2018). "Hydrodynamics of electrons in graphene." *J. Phys.: Condens. Matter* **30**, 053001.

[9] Majumdar, A. *et al.* (2025). "Universal quantum critical transport in graphene." *Nature Physics* (2025).

[10] Maldacena, J., Shenker, S. H., and Stanford, D. (2016). "A bound on chaos." *J. High Energy Phys.* **08**, 106.

[11] Müller, M., Schmalian, J., and Fritz, L. (2009). "Graphene: A nearly perfect fluid." *Phys. Rev. Lett.* **103**, 025301.

[12] Sulpizio, J. A. *et al.* (2019). "Visualizing Poiseuille flow of hydrodynamic electrons." *Nature* **576**, 75–79.

[13] Tu, S. and Das Sarma, S. (2023). "Wiedemann–Franz law violation in graphene." *Phys. Rev. B* **107**, 085401.

[14] Zaanen, J. (2019). "Planckian dissipation, minimal viscosity and the transport in cuprate strange metals." *SciPost Phys.* **6**, 061.

Contact: Carmichjaerladv@protonmail.com · 407-758-5512